Advances in Water Resources 31 (2008) 1470–1480

Contents lists available at ScienceDirect

Advances in Water Resources

journal homepage: www.elsevier.com/locate/advwatres

Estimation of rainfall fields using commercial microwave communication networks of variable density

Artem Zinevich [a,*], Pinhas Alpert [b], Hagit Messer [c]

[a] The Porter School of Environmental Studies, Tel-Aviv University, 69978 Tel-Aviv, Israel
[b] Department of Geophysics and Planetary Sciences, Tel-Aviv University, 69978 Tel-Aviv, Israel
[c] School of Electrical Engineering, Tel-Aviv University, 69978 Tel-Aviv, Israel

ARTICLE INFO

Article history:
Received 5 July 2007
Received in revised form 31 January 2008
Accepted 24 March 2008
Available online 8 April 2008

Keywords:
Microwave
Backhaul
Link
Rainfall
Tomography

ABSTRACT

The use of commercial microwave radio networks which are a part of cellular communication infrastructure for mapping of the near-the-ground rainfall is challenging for many reasons: the network geometry in space is irregular, the distribution of links by frequencies and polarizations is inhomogeneous, and measurements of rain-induced attenuation are distorted by quantization. A non-linear tomographic model over a variable density grid is formulated, and its applicability and performance limits are studied by means of a simulated experiment using a model of a real microwave network. It is shown that the proposed technique is capable to accurately measure integrated near-the-ground rainfall amounts over the area of 3200 km^2 with a bias smaller than 10%. In urban area, where the density of microwave links is high, the average correlation in space between the simulated model and reconstructed rainfall fields reaches 0.89 over the variable density grid with average cell size of 5.7 km^2 and 0.74 when interpolated into the rectangular grid with pixel size 0.775×0.775 km^2, for the quantization interval of 0.1 dB.

1. Introduction

The use of commercial microwave communication links which are a part of cellular telephony infrastructure for estimation of precipitation [1,2] is advantageous for many reasons: they are widespread over the world, fixed, line-of-sight and operate at frequencies of tens GHz, where precipitation is the major source of interruptions, resulting in attenuation of the received signal. Moreover, terrestrial microwave links (or backhaul links, connecting cellular towers back to a core network) are typically located a few tens of meters above the ground, providing therefore a useful facility for measurements of near-surface precipitation. Such links form dense networks and employ power control facilities for monitoring of network performance and adjusting power to assure undisturbed reception. These automatic power control systems require routine measurements of Received Signal Level (RSL) by receivers. Records of transmitted and received power, reflecting rainfall-induced attenuation A (dB km^{-1}) are collected at a control center and naturally allow estimation of average rain rate R (mm h^{-1}) per link based on the well-known power-law attenuation equation [3]:

$$A = aR^b \tag{1}$$

where the coefficients a and b are, in general, functions of frequency, polarization and drop size distribution (DSD) [4].

It has long been known that nearly linear relation of microwave attenuation A to rainfall R at wavelengths of 1 cm could serve as a basis for measurements of path-integrated and area-integrated rainfall [4–6]. The recent advances in communication technology enabled use of off-the-shelf commercial microwave equipment to measure near-the-ground rainfall. Thus, the advantage of microwave links for high temporal resolution measurements over conventional rain gauges was demonstrated in [7]. The use of dual-frequency links, operating at different, specially selected frequencies, allows estimation of rainfall rate as a linear function of ratio of two attenuations, lowering the effects of unknown DSD and producing reliable estimates of path-integrated rainfall [8,9] and rainfall spatio-temporal distribution, in conjunction with rain gauges and radar [10]. Following these findings, a number of applications of microwave measurements were explored. Thus, the advantages of use of single-frequency links for urban rainfall measurements were shown in [11]; others include calibration of weather radar [12], a two-steps procedure for correction of X-band radar attenuation and resulting rainfall estimates [13], identification of melting snow [14] and even estimation of DSD parameters [15].

The use of microwave attenuation measurements for tomographic reconstruction of rainfall fields was pioneered by Giuli et al. [16,17] who suggested a specially designed hypothesized system of microwave links with a predefined geometry, operating at specially selected frequencies where the A–R relationship is linear,

---

[*] Corresponding author.
E-mail address: artemsin@post.tau.ac.il (A. Zinevich).

0309-1708/$ - see front matter © 2008 Elsevier Ltd. All rights reserved.
doi:10.1016/j.advwatres.2008.03.003

combined with point rain gauges. This system allowed application of linear tomography to reconstruct spatial distribution of rainfall.

The existing approaches, however, heavily rely on dedicated equipment. The use of commercial hardware installations poses new challenges because commercial microwave networks are optimized for high communication performance and are designed in the way that reduces the effect of weather-related impairments on quality of service. Thus, the observation type, time and magnitude resolution, network geometry and frequencies are predefined and, in most cases, cannot be changed.

While some systems allow direct attenuation measurements at the temporal resolution of 1 min, others are designed to only measure minimum and maximum RSL for the 15-min time interval [1], or one instantaneous value each 15 min [2]. Time resolution for old equipment can even be worse, e.g. once per day measurements of minimum RSL. Power resolution (quantization) depends on specific equipment and may vary from 0.1 dB to several dB, which can result in large errors. The attenuation measurement error in estimation of integrated rainfall over a link [18] in presence of Δ dB quantization does not exceed $\Delta/2$. Therefore, the maximum error can be estimated according to (1) as

$$\delta R = \left(R^b + \frac{\Delta}{2aL}\right)^{\frac{1}{b}} - R \qquad (2)$$

In Fig. 1, we show simulation of maximum error in estimation of average rainfall due to $\Delta = 1$ dB quantization as a function of link frequency and length, according to [19].

Other difficulties in estimation of average rainfall per link from signal attenuation include uncertainties due to variability of DSD along the link [20], wet antenna attenuation [2] and uncertainty in determination of clear air attenuation due to water vapor-induced attenuation and scintillation effects [8,9].

Next, the geometry of the system of links is arbitrary, and the spatial resolution of the precipitation measurements is therefore determined by a given link topology. The analysis of a real microwave link network from an Israeli cellular provider (249 links, covering Israeli coastal plain which is discussed in the paper) shows that link density is highly variable – from 3 links per km^2 in urban areas up to 0.3 in rural ones.

Finally, the power-law equation (1) is non-linear at the frequency bands of 8, 18, 23 and 38 GHz – typical frequency bands used for communications; it is impossible to use linear tomography, since each link, in general, operates at its own frequency. It was demonstrated [6] that at the frequencies of about 35 GHz, the power-law relationship is approximately linear and is essentially independent on DSD and temperature, showing empirical errors of less than 10%. However, the uncertainties in determination of path-averaged rainfall intensity due to variation in DSD increase with lowering the frequency, reaching more than 20% at the frequencies of about 9 GHz. On the other hand, it was found in [15] that the instantaneous estimates based on the power-law equation (1) tend to overestimate the actual rainfall rate, especially at intense rain rates, where variations in DSD affect the power-law measurements, even though the agreement between power-law and dual-frequency estimates is very good during intervals of stratiform rain.

The aim of this paper is to demonstrate the potential of the commercial microwave communication links in large-scale rainfall measurements using a model of a real microwave system. We propose a non-linear tomographic model over a variable cell size grid and conduct a simulated experiment to obtain quantitative estimates of the major effects which are specific for commercial microwave networks – irregularity of the network topology, observation quantization and non-linearity of the power-law equation for different links, constituting the network.

2. Tomographic model

We formulate a non-linear tomographic model, where each link i is characterized by power-law coefficients a_i, b_i, corresponding to the link's frequency.

Suppose we have a set of observed rainfall-induced RSL attenuations A_i, $i = 1, \ldots, m$ from m wireless links of length L_i each one. Using (1), we obtain m expressions, relating the observed A_i with path-averaged rainfall R_i for the ith link [6]:

$$A_i = a_i R_i^{b_i} L_i = a_i \int_{L_i} r(x)^{b_i} \mathrm{d}x, \quad i = 1, \ldots, m \qquad (3)$$

where $r(x)$ is the true instantaneous rainfall in the point x.

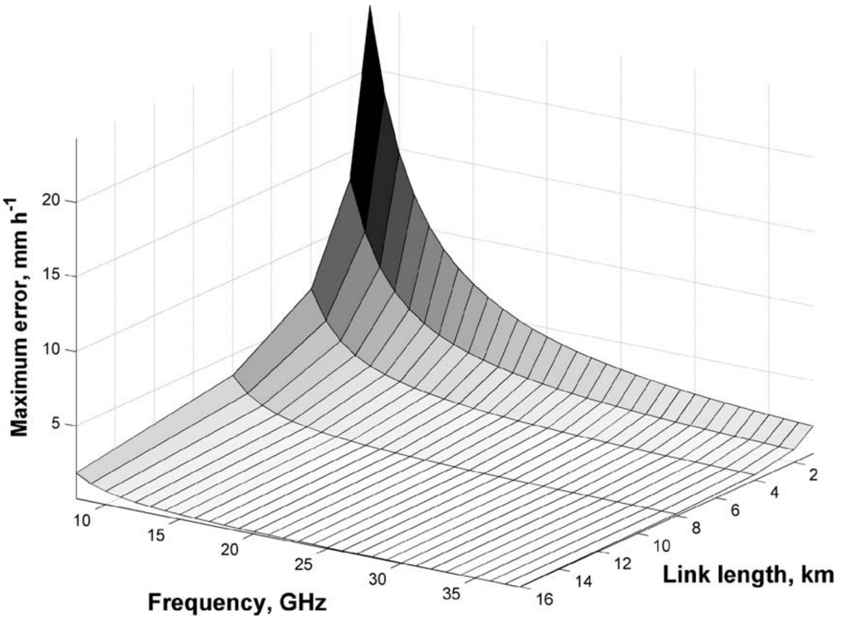

Fig. 1. Maximum rainfall estimation error due to 1 dB quantization as a function of link length and frequency, at the rain rate $R = 15$ mm h^{-1}.

Let us consider a 2D block model of the atmosphere where the whole region is divided into n small cells (pixels) and $\mathbf{r}$ is an n-vector of rainfall intensities. We make the following assumptions regarding the underlying rainfall field: (a) the rainfall intensity r_j, $j = 1, \ldots, n$ is assumed to be constant within each pixel (see Fig. 2) and (b) the rainfall field is smooth and its spatial correlation function takes the form [21]:

$$\rho(d) = c_0 \exp\left[-\left(\frac{d}{d_0}\right)^{s_0}\right] \tag{4}$$

Here, d is the separation distance between two points, c_0 is the correlation value for near-zero distances, accounting for local random errors in measurements, d_0 is the correlation distance ("scale parameter") and s_0 is the correlogram "shape parameter". The parameter c_0 was taken equal to one and the parameters d_0, s_0 are obtained by fitting [21] the model (4) with experimental spatial correlation values, estimated from a set of 26 radar rainfall maps (see Section 4 for the description of the event, considered in this study) over the $0.775 \times 0.775\ \mathrm{km}^2$ radar grid.

To formulate the tomographic equation, let l_{ij} be the length of the part of ith link passing through the jth pixel, so that $L_i = \sum_{j=1}^{n} l_{ij}$. Following the assumption (a), the system of equations (3) can be rewritten as

$$A_i = a_i R_i^{b_i} L_i \cong a_i \sum_{j=1}^{n} l_{ij} r_j^{b_i}, \quad i = 1, \ldots, m \tag{5}$$

and the system of m tomographic equations is, consequently, formulated as

$$f_i(\mathbf{r}) = \sum_{j=1}^{n} l_{ij} r_j^{b_i} - L_i R_i^{b_i} = 0, \quad i = 1, \ldots, m \tag{6}$$

From this system of equations it can be seen that the tomographic problem is inherently non-linear and the average rainfall intensity R_i depends on both rainfall intensities $\mathbf{r}$ and the power-law coefficient b_i. The system of equations (6) can be solved for unknown $\mathbf{r}$ by a variety of methods. Here we used the iterative Newton-Raphson method [22] for finding solution to the system of non-linear equations (6), where the problem is linearized at every iteration t. The algorithm consists of taking two first terms of Taylor series expansion of $\mathbf{f}$ (a vector of function f_i, $i = 1, \ldots, m$) and results in a linear matrix equation:

$$J_t \cdot \delta\mathbf{r}_{t+1} = -\mathbf{f}(\mathbf{r}_t) \tag{7}$$

where for every t, $J_{ij} = \partial f_i(\mathbf{r})/\partial r_j$ is the Jacobian matrix and the updated estimate of rainfall is $\mathbf{r}_{t+1} = \mathbf{r}_t + \delta\mathbf{r}_{t+1}$. One necessary requirement of the method is that the functions $\mathbf{f}$ should be continuously differentiable, that is in general not true for $b_i < 1$ (for example, for a horizontally-polarized link, operating at frequencies above 24 GHz according to [19]). The matrix J involves derivatives of $r_j^{b_i}$ in the form of $b_i r_j^{b_i - 1}$. In this case, these derivatives do not exist for $r_j = 0$, which should be taken into account. Another limitation of the linearization technique is that its convergence properties depend on initial guess. We initialized the rainfall field as $r_0 = 0.001\ \mathrm{mm\ h^{-1}}$.

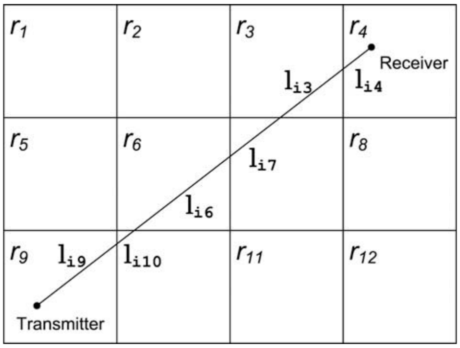

Fig. 2. A 2D block model of atmosphere. A wireless link is established from the cell 9 to the cell 4.

When dealing with an irregular microwave network and $m < n$, this inverse problem is underdetermined and requires some regularization. Here, we seek for a smooth solution answering the observations. To perform the linear inversion, we use SIRT – simultaneous iterative reconstruction technique [23], embedded into the inversion procedure:

$$\delta\mathbf{r}_{t+1}^{(k+1)} = \delta\mathbf{r}_{t+1}^{(k)} + N^{-1} J_t^{\mathrm{T}} D_t^{-1} \left(-\mathbf{f}(\mathbf{r}_t) - J_t \cdot \delta\mathbf{r}_{t+1}^{(k)}\right) \tag{8}$$

where k is the SIRT iteration index, N is a diagonal matrix whose components N_{jj} are numbers of links passing through the pixel j, and D is the diagonal matrix whose components are $(D_t)_{ii} = (J_t J_t^{\mathrm{T}})_{ii}$.

Note that the matrices D and N are invertible only if there is at least a part of a link passing through each pixel $j = 1, \ldots, n$. All "empty" pixels should be therefore excluded from the reconstruction procedure. After reconstruction, the rainfall in the "empty" pixels can be estimated from their neighbors, using interpolation by cubic splines, see Section 3. It can be shown [24] that the sequence $r_t^{(k)}$ converges to one of the infinite number of solutions of $J_t^{\mathrm{T}} J_t \cdot \delta\mathbf{r}_{t+1} = -J_t^{\mathrm{T}} \mathbf{f}(\mathbf{r}_t)$, which depends on the initial $\mathbf{r}_{t+1}^{(0)}$. We modify this procedure by adding a smoothing operator S, introducing correlation between neighboring pixels: $\mathbf{r}_t^{(k)} \to S \cdot \mathbf{r}_t^{(k)}$. The idea behind this smoothing-constrained inversion [25] is that, rather than fitting experimental data as well as possible which maximizes the roughness of the model, a smooth model which fits the data to within expected tolerance is sought. The $n \times n$ matrix $S = [\mathbf{s}_1, \mathbf{s}_2, \ldots, \mathbf{s}_n]^{\mathrm{T}}$ is constructed from the $n \times n$ distance matrix $D = [\mathbf{d}_1, \mathbf{d}_2, \ldots, \mathbf{d}_n]^{\mathrm{T}}$, which members $(D)_{ji} = d_{ji}$ are distances from pixel i to pixel j:

$$\mathbf{s}_j = [\rho(\mathbf{d}_j)]^{\gamma} \Big/ \sum_{i=1}^{n} [\rho(d_{ji})]^{\gamma} \tag{9}$$

where ρ is the spatial correlation function of rainfall given by (4) and $\gamma \geqslant 0$ is the "decorrelation power". When setting $\gamma \ll 1$, the smoothing is maximal since the operator S just averages all observed rainfall $\mathbf{r}$; when setting $\gamma \gg 1$, S approaches the identity operator, and no smoothing takes place. The optimal γ is determined experimentally, see Section 4.

The entire inversion algorithm can be formulated as follows:

(1) *Initialization:* Set $t = 1$, $\mathbf{r}_{t-1} = 0.001\ \mathrm{mm\ h^{-1}}$.
(2) *Linearization:* Calculate J_t.
(3) *Inversion:* Perform linear inversion of (7) by iterating (8) through k and, at each iteration, constraining the solution to be positive and applying the smoothing operator S. Pixels below zero are replaced by white noise with mean and standard deviation $0.05\ \mathrm{mm\ h^{-1}}$, to push the estimates away from an incorrect negative solution. The resulting values are clipped to minimum $0.001\ \mathrm{mm\ h^{-1}}$. Iterations continue unless the condition $\|\delta\mathbf{r}_t^{(k+1)} - \delta\mathbf{r}_t^{(k)}\| < \epsilon_k$ is met.
(4) *Stop condition:* The reconstruction procedure finishes when the stopping criterion $\|\mathbf{r}_{t+1} - \mathbf{r}_t\| < \epsilon_t$ is met; otherwise, the linearization process continues (set $t = t + 1$, move to step 2).

In practice, this linearization procedure is very accurate and converges fast (typically in 3–4 iterations). However, when quantization noise is added to simulation, the linearization is less accurate, as illustrated by simulation results, presented in Section 4.

3. Variable cell size grid

A conventional rectangular grid, used in the most tomographic applications, does not fit the networks whose link density varies in space; with the uniform grid, spatial resolution is determined by sparse areas (every pixel of any grid should be crossed by at least a part of one link), loosing the advantage of dense parts of a link network.

The density of such variable density grid should follow the spatial distribution of microwave links (the denser network, the smaller reconstruction cells), and the cells themselves should be as much isometric as possible. To formulate the data-driven grid building procedure, we firstly need to represent the microwave network in a convenient form. Assuming that each part of every link of the length $\Delta l \to 0$ carries a portion of information about the rainfall field, we consider each link as a union of n_w intervals and represent each interval as a point in space, according to the coordinates of the interval center. The whole network of m links is therefore represented as a set of data points $\Omega = \{\mathbf{w}_k\}$, $k = 1, \ldots, m \times n_w$, where each $\mathbf{w}_k$ is a 2-vector of coordinates of the kth point. The assumption behind such representation of an interval by a point is that the rainfall intensity is constant in the circle of radius $\Delta l/2$ around the point, which is plausible for $\Delta l < 0.775$ km (the spatial resolution of the model, used for simulation, see Section 4; in real applications, the maximum Δl should be chosen according to the spatial correlation properties of local rainfall patterns). Since link lengths L_i, $i = 1, \ldots, m$ in our experimental setup do not exceed 27 km, we have chosen $n_w = 35$.

We propose here a variable density reconstruction grid, which is optimized for a specific microwave link installation to fit the cellular backhaul network. The data-driven algorithm for building of reconstruction grid is formulated as an iterative top-down tree growing procedure, where at each iteration a subset of the most populated (by links) cells is selected for binary split. To supply the desired properties to the data-driven grid, we adopt the K-means clustering algorithm [26], described below.

The algorithm finds a locally optimal partition $\{C_1, \ldots, C_K\}$ of the database Ω to minimize the sum of Euclidian distance between each element of Ω and its nearest cluster center (*centroid*) C_i, $i = 1, \ldots, K$:

$$\{C_1, \ldots, C_K\} = \arg\min_{P_K(\Omega)} \sum_{i=1}^{K} \sum_{j=1}^{K_i} \|\mathbf{w}_{ij} - \bar{\mathbf{w}}_i\|^2 \tag{10}$$

where K is the number of clusters, $P_K(\Omega)$ is a set of all the partitions of the database Ω into K non-empty clusters, K_i is the number of objects of the cluster i, $\mathbf{w}_{ij}$ is the jth data point of the ith cluster and $\bar{\mathbf{w}}_i$ is the centroid of the ith cluster, that is defined as

$$\bar{\mathbf{w}}_i = \frac{1}{K_i} \sum_{j=1}^{K_i} \mathbf{w}_{ij}, \quad i = 1, \ldots, K \tag{11}$$

The K-means algorithm is summarized as follows:

(1) *Assignment:* Find for each data point its closest cluster centroid. Then, if a cluster has no data points assigned (which means that there is no link crosses the cell, represented by this centroid), the cluster is removed from the current partition. This way it is assured that each cluster is crossed by at least a part of a link.
(2) *Calculation:* For each cluster $i = 1, \ldots, K$, estimate $\bar{\mathbf{w}}_i$ as a center of masses of its data points according to Eq. (11).
(3) *Stop condition:* Stop if there was no move of data points between clusters since last iteration. Otherwise, move to step 1.

Since the number of points n_w is the same for all links, the data points, corresponding to short links are closer to each other in space relatively to longer links, and therefore shorter links receive higher weight in the clustering procedure (for example, two short

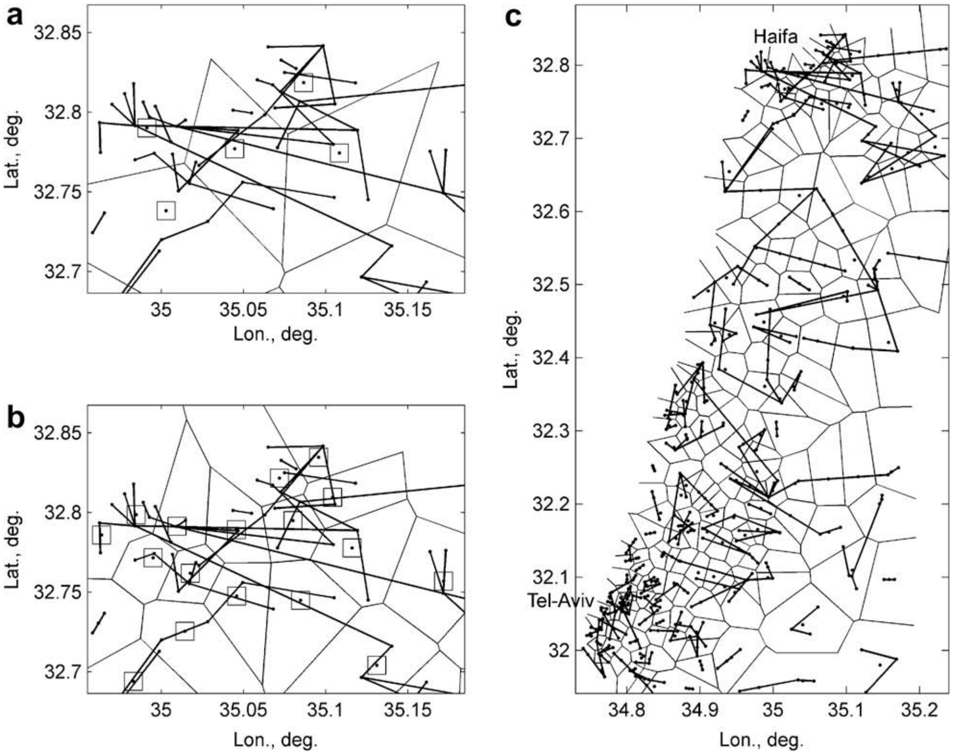

Fig. 3. Voronoi charts showing (a, b) different stages of building of the variable density grid (squares are cell centers) and (c) the resulting grid used for simulations, consisting of 193 clusters for 249 links of a real microwave network along the Israeli coastal plain.

links of length L_1 and L_2 carry more information about the spatial distribution of rainfall than one longer link of the length $L_1 + L_2$).

The complete iterative (through t) tree growing procedure is described below:

(1) *Initialization:* Set $t = 1$ and create an initial partition, consisting of a single centroid C_{1t} with coordinates $\bar{\mathbf{w}}_1$ ($K^{(t)} = 1$), which is calculated as a center of masses of all data points, representing the network.

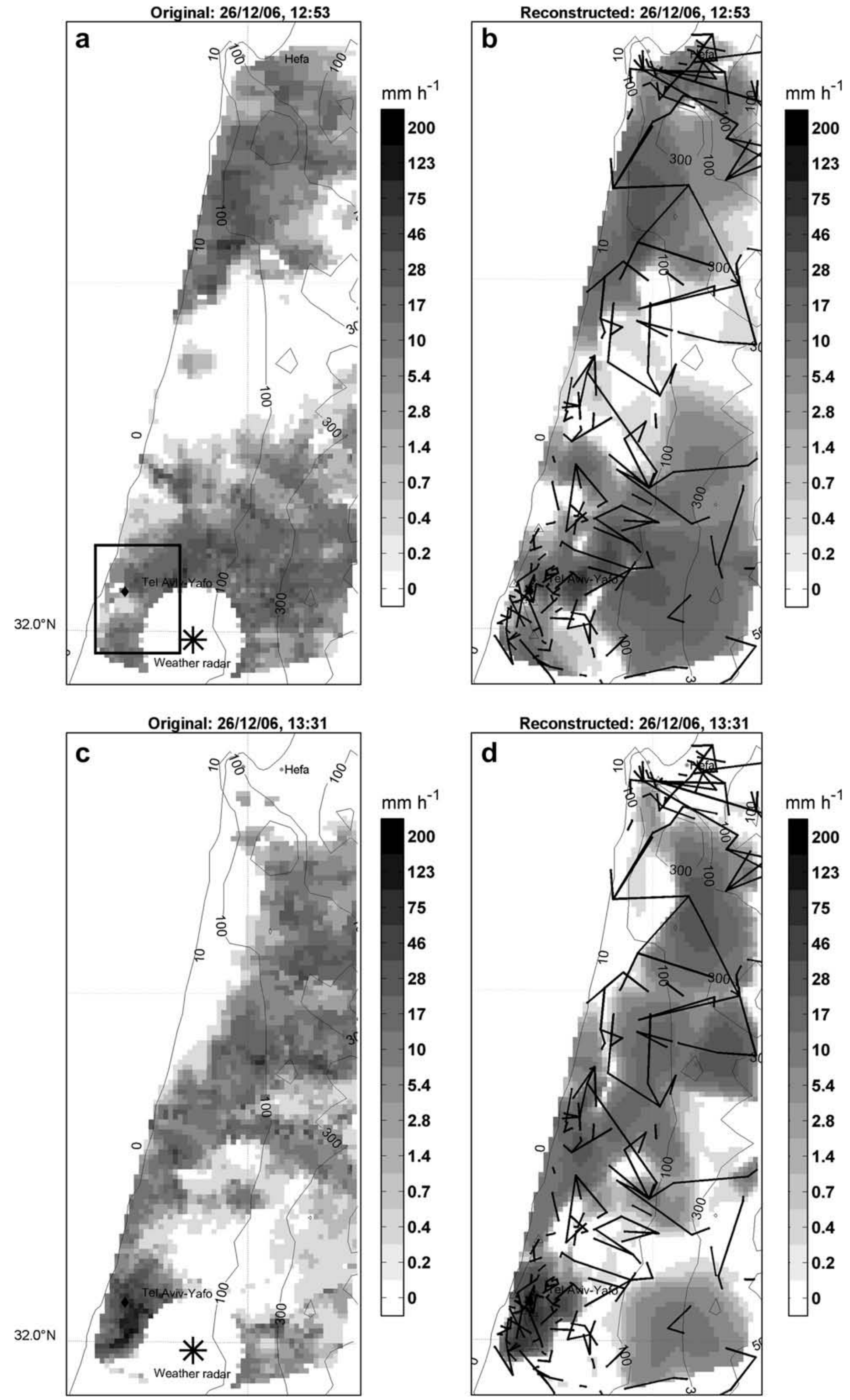

Fig. 4. Rainfall fields at two time slots (a, b) and (c, d). Figures (a, c) show original (model) rainfall, (b, d) – tomographic reconstruction with 0.1 dB quantization. Tel-Aviv area is indicated by the rectangle in (a).

(2) *Splitting:* At each tree growing iteration t, all clusters which have data points from two and more crossing links are selected for binary split. Then, each selected centroid i is split into two along the dimension with the highest variance of data points distribution:

$$C_i \to \{C_{i1}, C_{i2}\}, \quad \bar{\mathbf{w}}_i \to \{\bar{\mathbf{w}}_i + \boldsymbol{\delta}_i, \bar{\mathbf{w}}_i - \boldsymbol{\delta}_i\}, \qquad i = 1, \ldots, K \quad (12)$$

$$\boldsymbol{\delta}_i = \boldsymbol{\sigma}_i \cdot \begin{cases} [1,0]^{\mathrm{T}}, & \sigma_{i1} > \sigma_{i2} \\ [0,1]^{\mathrm{T}}, & \text{otherwise} \end{cases}, \qquad i = 1, \ldots, K \qquad (13)$$

$$\boldsymbol{\sigma}_i = [\sigma_{i1}, \sigma_{i2}]^{\mathrm{T}} = \left[\frac{1}{K_i}\sum_{j=1}^{K_i}(\mathbf{w}_{ij} - \bar{\mathbf{w}}_i)^2\right]^{1/2}, \qquad i = 1, \ldots, K \qquad (14)$$

(3) *Re-clustering: K*-means algorithm is executed for the new partition with splitted cluster centroids, producing a new grid with $K^{(t+1)}$ clusters.

(4) *Stop condition:* If the desired grid size K^d is reached ($K^{(t+1)} \geqslant K^d$), stop iterations. Otherwise, continue tree growing (set $t = t + 1$, move to step 2).

The algorithm of tree growing is therefore a sequence of splits, followed by *K*-means clustering after each one.

The optimal grid size $K^d = 193$ (Fig. 3c) is determined experimentally (see Section 4). Examples of intermediate iterations of the tree growing procedure are shown at Fig. 3a and b. Since we are interested in the estimation of the rainfall intensity for every point in space, the reconstruction over the variable density grid should be followed by interpolation of obtained results into the rectangular grid with a predetermined pixel size. Here, we choose to use 2D cubic interpolation, which is based on triangulation of an irregularly spaced set of points, and consists of finding curved triangular shapes, whose slopes on both sides of each boundary can be made equal. This method provides a surface with continuous first and second derivatives which can be considered as an adequate representation of a smoothed rainfall field if interpolated locally, i.e. the triangles are as close as possible to equilateral (for details, see [27]). This, however, is not always possible; thus, the triangles may be poorly shaped (thin and elongated), for example, if the outermost data points form a concave set near a boundary of the monitored area (see Section 5). To eliminate the resulting artifacts, we bounded the reconstruction area by a set of 400 equally spaced zero rainfall data points, providing this way the zero rainfall boundary condition for the interpolation procedure.

4. Simulated experiment

In order to evaluate the performance limits of the system, we have conducted a simulated experiment, using a model of a real commercial microwave network, including 249 microwave links of lengths 0.5–27 km operating at 8–38 GHz, both vertically and horizontally polarized. This network is located along the Israeli coastal plain, covering the area of about 3200 km^2. Presently, the controlling software of this microwave network is capable to sample the minimum RSL only once per day, which limits its applicability for practical rainfall measurements. However, the wide coverage of the network and attractive hardware properties (the magnitude resolution of the equipment is 0.1 dB) allows us to consider it as a potentially powerful facility for rainfall measurements in Israel and a convenient test bed, representing microwave link spread over urban and suburban areas, to evaluate the proposed tomographic reconstruction algorithm and to simulate the effects of variable link density, real frequency distribution (in general, the longer the links, the lower the frequency) and quantization error.

We derived the simulated rainfall fields from radar measurements of real rainfall events, collected by Shacham weather radar installed near Ben Gurion Airport. The observed reflectivity data was converted to the rain rates using the standard Z–R relationship and was used as a model of "ground truth" for the simulated experiment, taking advantage of radar ability to reflect well spatial and temporal variability of rainfall (a similar approach was used, for example, in [17]), at the spatial resolution (the size of radar pixel) of 0.775×0.775 km^2 and temporal resolution (the average antenna rotation period) of 5.2 min, for a 2-h strong convective rainfall event on 26 December 2006 11:49–14:00, 26 time slots overall. The whole simulation experiment consists of:

1. Extraction of rainfall maps from radar data.
2. Calculation of attenuation of all microwave links according to their frequencies, polarizations, lengths and the simulated rainfall field, using the power-law attenuation equation (1). The measurement errors were simulated as a zero-mean Gaussian noise with variance equal to 5% of the measured value, uncorrelated between different links [16]. Afterwards, the estimated attenuation values were quantized at magnitude resolution of zero, 0.1 and 1 dB, to simulate the effects of analog-to-digital discretization, introduced by a real receiver hardware. The choice of the coefficients a and b of the power-law equation should not necessarily be optimized for local climatological conditions for the simulation purposes, so we used the ones recommended in [19].
3. Spatial reconstruction of rainfall fields from the simulated observations, using our proposed non-linear tomographic model over the variable cell size grid.
4. Comparing the reconstructed fields with the original radar data. The knowledge of the "ground truth" in the simulated experiment allows to obtain quantitative estimates of the reconstruction accuracy as well as to examine the specific effect of the quantization distortion.

To get insight into the dependence of error on the density of links, we calculated performance statistics over two regions: the whole Israeli coastal plain including very sparse regions and the Tel-Aviv city area where the density of microwave links is at its highest (see Fig. 4a, Table 1).

Since the density of links (and, consequently, the reconstruction cell size) is highly variable in space, we are interested in evaluating the reconstruction algorithm at different spatial scales:

1. *Reconstruction scale:* The spatial resolution of the measurement system is predetermined by the network topology (at every cell, the tomographic algorithm estimates the average rainfall) and, therefore, the natural scale for the quantitative performance estimation would be the one corresponding to the grid pattern. For comparison with reconstructed rainfall fields, we estimated the average model rainfall over the variable density grid. Note that while such comparison is useful in terms of analyses of the algorithm, it gives equal weights to the pixels of different sizes, and hence performance analyses in this scale is not relevant for practical applications where measuring of integrated rainfall amounts over an area is of interest.

Table 1
Characteristics of different areas where the performance of the tomographic reconstruction was evaluated

	Coastal plain	Tel-Aviv area
Area (km^2)	3200	184
Number of links	249	68
Average cell size (km^2)	16.5	5.7

(2) $0.775 \times 0.775\ \mathrm{km}^2$ *scale:* We interpolate the reconstructed rainfall fields back into the radar rectangular grid, giving this way proper weighting of observations proportional to the area, occupied by every pixel, using 2D bicubic spline interpolation over the non-uniform grid.

In this study, we focus on two aspects which are relevant to the performance evaluation [17].

(1) *General performance of the monitoring system:* The purpose of these statistics is to evaluate the quality of estimation of rainfall distribution in space. We denote the "ground truth" model rainfall in the pixel $j = 1, \ldots, n$ at the time $t = 1, \ldots, T$ as r'_{jt} and the reconstructed rainfall as r_{jt}. For each one of two evaluation areas, we calculate the correlation coefficient ρ_s, normalized bias $\mathrm{NBias_s}$ and normalized bias-corrected root mean squared error $\mathrm{NRMSE_s}$ [28,29] (the subscript s stands for *spatial*), averaged over $T = 26$ time frames:

$$\rho_s = \frac{1}{T}\sum_{t=1}^{T} \frac{\sum_{j=1}^{n}(r_{jt} - \bar{r}_t)(r'_{jt} - \bar{r}'_t)}{\left[\sum_{j=1}^{n}(r_{jt} - \bar{r}_t)^2 \sum_{j=1}^{n}\left(r'_{jt} - \bar{r}'_t\right)^2\right]^{1/2}} \tag{15}$$

$$\mathrm{Bias_s}(t) = \frac{1}{n}\sum_{j=1}^{n}(r_{jt} - r'_{jt}), \tag{16}$$

$$\mathrm{NBias_s} = \frac{1}{T}\sum_{t=1}^{T}\left[\mathrm{Bias_s}(t) \Big/ \left(\frac{1}{n}\sum_{j=1}^{n} r'_{jt}\right)\right] \tag{17}$$

$$\mathrm{RMSE_s}(t) = \left[\frac{1}{n}\sum_{j=1}^{n}(r_{jt} - r'_{jt} - \mathrm{Bias_s}(t))^2\right]^{1/2} \tag{18}$$

$$\mathrm{NRMSE_s}(t) = \frac{1}{T}\sum_{t=1}^{T}\left[\frac{\mathrm{RMSE_s^2}(t)}{\frac{1}{n}\sum_{j=1}^{n}(r'_{jt} - \bar{r}'_t)^2}\right]^{1/2} \tag{19}$$

where $\bar{r}'_t$ and $\bar{r}_t$ are average precipitation intensities of the model and of the reconstruction, respectively, at the time frame t. The necessity to normalize the statistics rather than present the absolute error values arises from our desire (a) to compare performance in different areas (whole coastal plain and Tel-Aviv area) where the average rainfall differs (only two hours of data were used), and (b) to asses the algorithm performance in the scale that gives a clear meaning to the 100% error. Thus, for the correct reconstruction, $\mathrm{NBias_s}$ should be close to zero; $\mathrm{NBias_s} = 1$ corresponds to the case when all rainfall is missed, and becomes negative if the algorithm overestimates the actual rainfall. The bias-corrected $\mathrm{NRMSE_s}$ statistics (equal to the normalized standard deviation of error) indicates the ability of the algorithm to estimate the variability of the estimated rainfall over either space or time, which is not represented by $\mathrm{NBias_s}$. The practice of normalizing RMSE by the average rainfall can be inappropriate in cases when the rainfall intensity is estimated over large areas which can include large spaces with no rain. In these cases, the average rainfall can be rather low, and the meaning of such normalized RMSE is unclear. Here we normalize RMSE by the standard deviation of the time series that has a simple interpretation: $\mathrm{NRMSE_s}$ is close to one for any "constant" result, e.g. any estimate of rainfall that is the same for all pixels and does not reflect the spatial variability of rainfall.

(2) *Accuracy of estimation of the mean rainfall rate over an area:* In this case we asses the performance of the approach in time, rather than space. We used here ρ_t, $\mathrm{NBias_t}$ and $\mathrm{NRMSE_t}$ (the subscript t stands for *temporal*) statistics. At the time frame t, $t = 1, \ldots, T$ the "ground truth" and the reconstructed average areal rainfalls are calculated as $r'_t = \frac{1}{n}\sum_{j=1}^{n} r'_{jt}$ and $r_t = \frac{1}{n}\sum_{j=1}^{n} r_{jt}$, respectively. The statistics are then estimated as

$$\rho_t = \frac{\sum_{t=1}^{T}(r_t - \bar{r})(r'_t - \bar{r}')}{\left[\sum_{j=1}^{T}(r_t - \bar{r})^2 \sum_{t=1}^{T}(r'_t - \bar{r}')^2\right]^{1/2}} \tag{20}$$

$$\mathrm{Bias_t} = \frac{1}{T}\sum_{t=1}^{T}(r_t - r'_t), \quad \mathrm{NBias_t} = \mathrm{Bias_t}/\bar{r}' \tag{21}$$

$$\mathrm{NRMSE_t} = \left[\frac{\sum_{t=1}^{T}(r_t - r'_t - \mathrm{Bias_t})^2}{\sum_{t=1}^{T}(r'_t - \bar{r}')^2}\right]^{1/2} \tag{22}$$

where $\bar{r}'$ and $\bar{r}$ are average precipitation intensities of the model and of the reconstruction result, respectively, over the whole period of length T.

We compare the performance of the reconstruction over the variable density data-driven grid with the rectangular grid with pixel size $4 \times 4\ \mathrm{km}^2$, to demonstrate the advantage of the former. The optimal pixel size was determined experimentally (see below). The reconstruction over the rectangular grid is possible only for pixels with at least one link crossing. For the rest of the area, the rainfall fields were estimated using exactly the same procedure of spatial interpolation as in the case of the data-driven variable density grid. The only difference between these experiments is the coordinates of the pixel centers, either according to the rectangular grid or the data-driven one. To validate the assumptions behind the linearization procedure and the Newton–Raphson method, we compared the simulation results to a linear model. In the linear model, both simulated observations and linear tomographic reconstruction (7) were calculated under the assumption of the power-law coefficient $b_i = 1$, $i = 1, \ldots, m$. A number of parameters of the procedure (the optimal number of reconstruction cells of the data-driven grid, the optimal pixel size of the rectangular grid and the smoothing parameter γ) were determined experimentally over one (at $t = 0$) of the 26 time frames according to the minimum reconstruction error $\mathrm{Bias_s}(t)^2 + \mathrm{RMSE_s}(t)^2$.

5. Results and discussion

The examples of rainfall fields, reconstructed using the non-linear model and simulating 0.1 dB quantization of observations, interpolated into the radar grid, are given at Fig. 4 for two different time slots. One can see that while the suggested approach is in general capable to reveal the major features of the rainfall spatial structure, its main shortcomings express in loss of fine details in the rural areas, where the density of links is low and the reconstructed rainfall map is smooth. Another effect is smoothing of extreme rain rates over the densest part of the network in Tel-Aviv, see Fig. 4d – even though the rain rates are very high (up to $70\ \mathrm{mm\ h^{-1}}$), the heavy rainfall areas are very limited in space and longer links inevitably smooth them.

The better understanding of capabilities and limitations of the technique one can gain from the maps of statistics (Fig. 5) – ρ_t, $\mathrm{NBias_t}$ and $\mathrm{NRMSE_t}$, calculated for every pixel (by taking $n = 1$) over the whole 2-h event. One can see that the best results in all statistics are obtained in dense Tel-Aviv area not including the radar clutter area, and the worst results are over near-boundary areas. Thus, the reason for low performance in areas i, ii in Fig. 5d is that the algorithm is unable to reconstruct correct rain fields in the regions which are only partially surrounded by links. In another words, this demonstrates a weakness of the zero rainfall boundary condition which is necessarily applied to allow interpolation over concave boundaries of the monitored area. The same effect for a single time slot can be observed in Fig. 4d. Area ii which

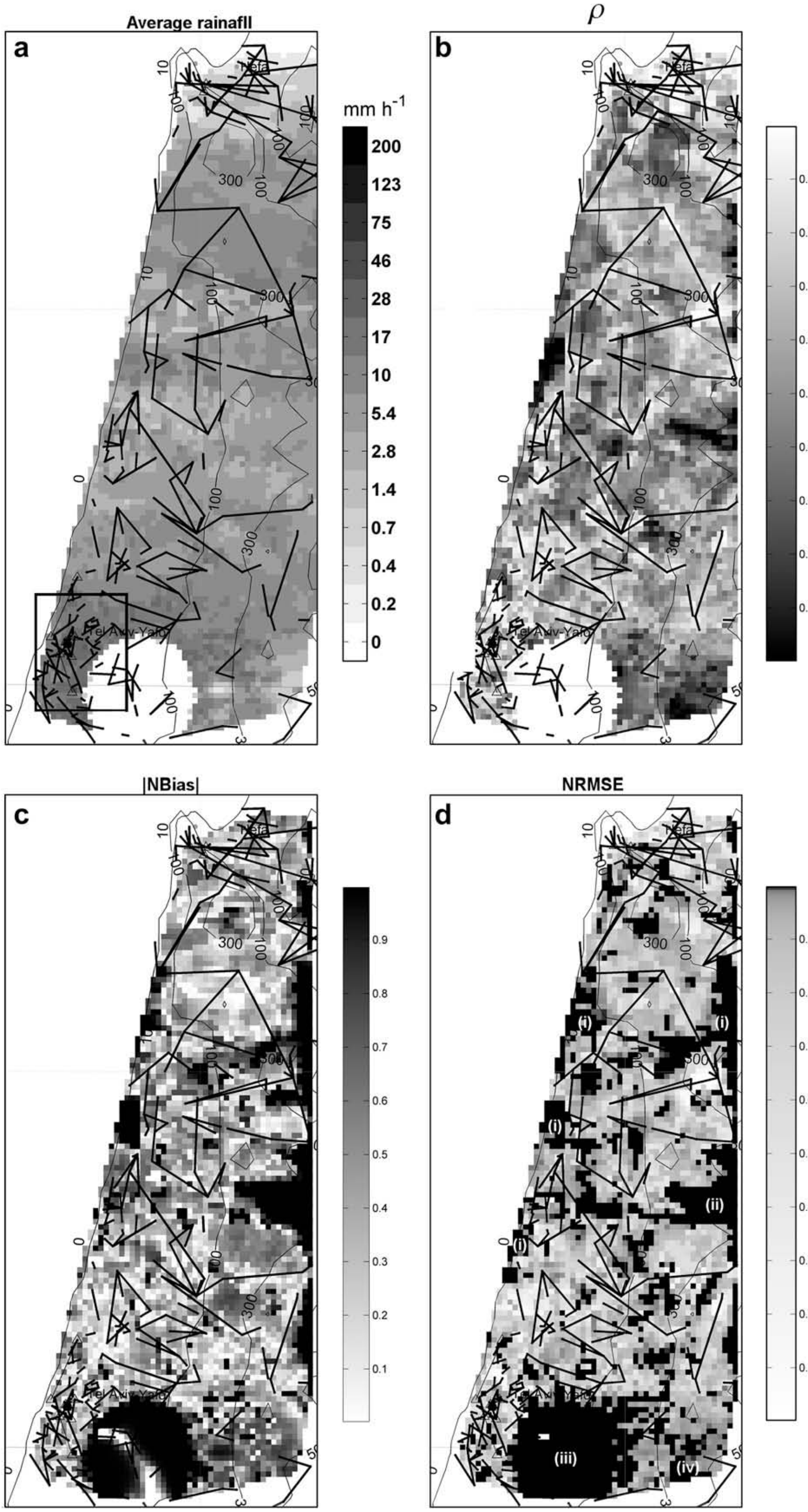

Fig. 5. The map of average rainfall intensity over the whole 2-h period (a) and maps of ρ_t (b), $|\mathrm{NBias}_t|$ (c) and NRMSE_t (d), for every point of the reconstructed space. The dark parts of the statistics maps correspond to the worst error statistics. The $|\mathrm{NBias}_t|$ and NRMSE_t statistics are limited to within the interval (0,1). In (a), Tel-Aviv area is indicated by the rectangle. In (d), some regions with severe NRMSE_t are labeled as i–iv and are discussed in the text. Note that the scale in (d) was changed to improve the visual appearance of the figure.

appears on all three statistics maps is in the largest data-void area where rainfall is consistently missed. The performance in the radar clutter area iii is severely distorted for two reasons. Firstly, the mean and the standard deviation of the model rainfall in this area is zero, so that ρ_t and normalized NBias_t and NRMSE_t cannot be estimated. On the other hand, abrupt changes of the model rainfall on the clutter boundary cannot be reconstructed by the relatively sparse network since the assumption of the smooth rainfall field is violated. This violation can clearly be seen in Fig. 4d. Local sporadic failures can be seen in Fig. 5b–d over the whole coastal plain, mostly in the regions with no links passed, which means that the microwave network is too sparse at these places (i.e. for large pixels, the assumption of the constant rainfall in a pixel is violated) to represent the fine features of the rainfall field according to the suggested method of building of the data-driven variable density grid and the SIRT inversion.

The scatter plots of the reconstructed rainfall (Fig. 6) of the 0.1 dB quantized non-linear simulation using the variable density grid provide another view on the performance of the technique. Each data point in the scatter plot represents the reconstructed rainfall intensity over a reconstruction cell vs. average model rainfall, calculated in the same grid cell from the model data. The linear plots in both monitored areas show that the regression equations are very close to 1:1 correspondence, which is in accordance with the low bias of the reconstruction (Tables 2 and 3). The same results are obtained with 1 dB quantization simulation.

The highest overall correlation of the whole dataset (193 reconstruction cells × 26 time slots) is achieved in Tel-Aviv region, reaching 0.92 for 0- and 0.1 dB quantization and 0.91 for 1 dB quantization simulation (0.86, 0.85, 0.84 for 0-, 0.1-, 1 dB quantization, respectively, for the whole coastal plain). The results of 0.1 dB quantized simulations exhibit systematic underestimation of rainfall rates below 1 mm h^{-1}, which can be observed on the log–log plot, Fig. 6. This is not surprising since the effect of low rain rates on quality of service of a microwave link is weak and is out of interest for equipment manufacturers. The 1 dB quantized simulation leads to even worse underestimation of weak rain rates, which is reflected in a detailed quantitative performance analysis, given below:

(1) *General performance.* The results of simulation for the reconstruction and radar grids are given in Tables 2 and 3. For the radar grid and 0.1 dB quantization, ρ_s is 0.77 and NRMSE_s is 0.65, for the coastal plain area. The reason for these relatively low results is that we compare results, obtained over the grid with average cell size of 16.5 km^2 with model at the 0.775×0.775 km^2 resolution. The reconstructed surface is much smoother, and small-scale rainfall features are frequently missed. As it can be seen from Tables 2 and 3, the model with the data-driven grid outperforms the rectangular grid in almost all cases, except for Table 2, where ρ_s in Tel-Aviv area reaches 0.9 for the rectangular grid. That demonstrates performance comparable to the data-driven grid; however, the smoothing effect of the 4×4 km^2 relatively to the data-driven grid in Tel-Aviv area expresses in higher NBias_s and NRMSE_s. Conversely, the rectangular grid in the most of the coastal plain area is too dense relatively to the sparse network outside Tel-Aviv area, which results in many grid cells, non-optimally distributed in space and poorly covered by the network. This requires increase of the smoothing parameter γ in order to achieve the minimum overall reconstruction error, which in turn results in oversmoothing in the dense parts of the grid in Tel-Aviv area. Such sub-optimality leads to overall worse performance, rel-

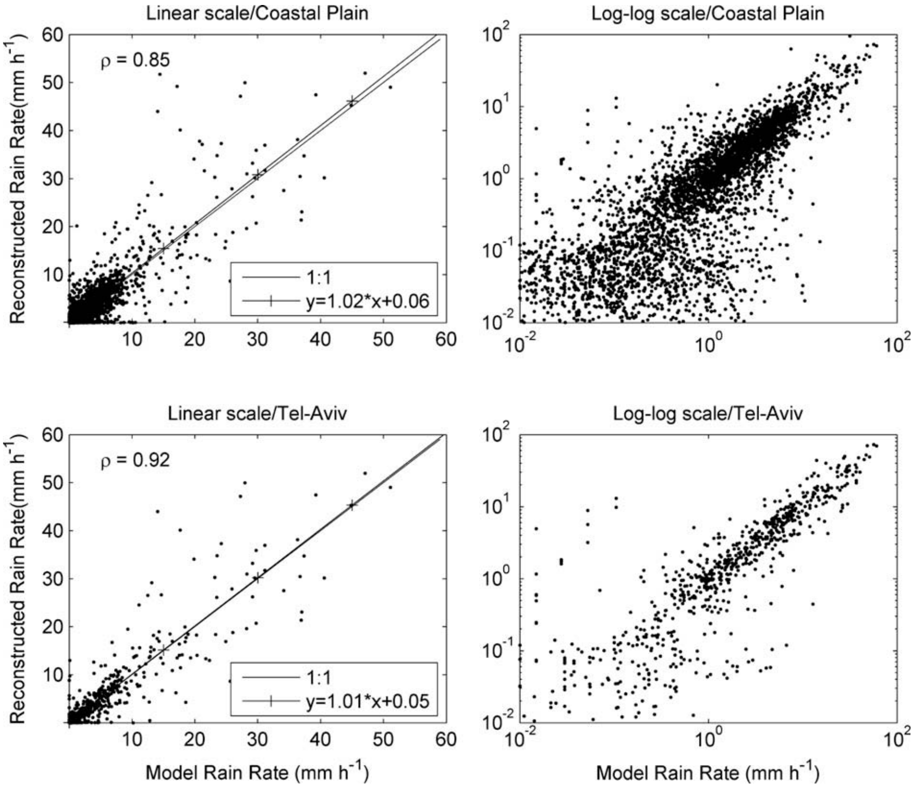

Fig. 6. Scatter plots and corresponding linear regression equations of the reconstructed rainfall fields for the non-linear model and 0.1 B quantization, in both linear and log–log scales, over the whole coastal plain and Tel-Aviv areas, in the reconstructed scale. On the log–log plots it can be seen that 0.1 dB quantization of observations results in systematic underestimation of model rain rates below 1 mm h^{-1}: most of reconstructed rain rates fall below 0.2 mm h^{-1}. The correlation coefficients are calculated over the whole dataset (193 reconstruction cells × 26 time frames) and therefore differ from ρ_t, ρ_s, appearing in the tables.

Table 2
The effects of model features (variable cell size grid, non-linear model, accounting for real link frequencies, and quantization error) on reconstruction performance, for the spatial statistics

Grid	Model	Quant.	Coastal plain			Tel-Aviv area		
			ρ_s	NBias$_s$	NRMSE$_s$	ρ_s	NBias$_s$	NRMSE$_s$
Rect.	Linear	No	0.79	0.07	0.83	0.90	0.10	0.62
Var.	Linear	No	0.83	0.06	0.70	0.90	0.04	0.54
Var.	Non-linear	0.1 dB	0.82	0.06	0.72	0.89	0.03	0.55
Var.	Non-linear	1 dB	0.79	−0.01	0.80	0.85	−0.09	0.65

Simulation results are in the reconstruction scale. Average cell size is 16.5 km^2 for the coastal plain area and 5.7 km^2 for Tel-Aviv urban area. Average rainfall intensities are 0.94 mm h^{-1} and 3.52 mm h^{-1}, respectively.

Table 3
The effects of model features on reconstruction performance, for the spatial statistics

Grid	Model	Quant.	Coastal plain			Tel-Aviv area		
			ρ_s	NBias$_s$	NRMSE$_s$	ρ_s	NBias$_s$	NRMSE$_s$
Rect.	Linear	No	0.59	−0.06	0.82	0.63	0.29	0.83
Var.	Linear	No	0.65	−0.04	0.76	0.75	0.10	0.67
Var.	Non-linear	0.1 dB	0.65	−0.04	0.77	0.74	0.10	0.68
Var.	Non-linear	1 dB	0.63	−0.08	0.80	0.71	0.00	0.72

The results are calculated over the rainfall fields, interpolated into 0.775 × 0.775 km^2 reconstruction grid.

atively to the data-driven variable density grid. The substantial difference in NBias$_s$, calculated over the whole coastal plain area between the reconstruction-scale grid (Table 2) and the radar grid (Table 3) reflects the underestimation of rainfall in the latter due to zero rainfall interpolation boundary conditions. Conversely, the positive NBias$_s$ in Tel-Aviv area is mostly due to overestimation of zero model rainfall in the radar clutter area. The contribution of the clutter area into the statistics becomes proportional to its area after interpolation (Table 3), hence the increase in positive NBias$_s$ in Tel-Aviv area relatively to the reconstruction grid (Table 2). In Tables 2 and 3, one can see that the performance results of the non-linear model (comprising power-law coefficients, corresponding to the real link frequencies) with 0.1 dB quantization are very close to the linear model (which does not account for real frequency distribution, assuming linear *A*–*R* relationship) with no quantization. Simulating 1 dB quantization gives, however, substantial performance decrease: lower correlation ρ_s, lower NBias$_s$, caused by missing weak rain rates, and increased NRMSE$_s$. Thus, in Table 3, in Tel-Aviv area NBias$_s$ reduces from 0.1 to 0.00 when changing quantization interval from 0.1 dB to 1 dB, i.e. the additional negative bias due to missed weak rain rates in the case of 1 dB quantization compensates the existing positive bias of the reconstruction. Note that the results in Tel-Aviv area are consistently better than in the whole coastal plain, which is most likely due to the difference in link density, rather than the difference in average rainfall intensity (3.52 mm h^{-1} in Tel-Aviv area vs. 0.94 mm h^{-1} over the whole coastal plain), since we use normalized statistics that do not depend on absolute rainfall strength. The better Tel-Aviv performance can be seen in all simulations regardless quantization interval (the quantization error depends on rain rate; low rain rates are affected more and can be completely missed). The average correlation in space ρ_s between model and reconstructed rainfall fields in the dense Tel-Aviv area reaches 0.75 over the 0.775 × 0.775 km^2 grid and 0.89 over the reconstruction scale grid, which confirms the potential applicability of the system for high-resolution measurements of rainfall in urban areas.

(2) *Mean rain rate estimation.* The results of estimation of average rainfall rate over large areas (ρ_t, NBias$_t$ and NRMSE$_t$) for rainfall, interpolated into the 0.775 × 0.775 km^2 grid are given in Table 4. The effects of the non-linear vs. linear model, data-driven vs. rectangular grid and observation quantization are very similar to ones of Tables 2 and 3. Note that the interpolation is necessary to give proper weighting to the reconstruction cells of different sizes when speaking about average areal rainfall (the non-interpolated results would be meaningless). The temporal correlation ρ_t of the time series of average rainfall over the whole area is high (relatively to ρ_s), reaching 0.96 for the whole coastal plain and 0.99 for Tel-Aviv area, for non-linear 0.1 dB simulation over the data-driven grid. It should be taken into account that ρ_t is calculated over only 26 members (time slots). The absolute NBias$_t$ in any case does not exceed 0.08 and the values of NRMSE$_t$ are considerably lower than NRMSE$_s$ that suggests the applicability of the method to measurements of integrated rainfall amounts over large areas. Similarly to NBias$_s$, increasing quantization to 1 dB leads to

Table 4
The effects of model features on reconstruction performance, for the temporal statistics

Grid	Model	Quant.	Coastal plain			Tel-Aviv area		
			ρ_t	NBias$_t$	NRMSE$_t$	ρ_t	NBias$_t$	NRMSE$_t$
Rect.	Linear	No	0.96	−0.06	0.27	0.98	0.14	0.24
Var.	Linear	No	0.96	−0.05	0.27	0.98	0.05	0.14
Var.	Non-linear	0.1 dB	0.96	−0.05	0.27	0.98	0.06	0.14
Var.	Non-linear	1 dB	0.97	−0.08	0.27	0.98	0.00	0.13

The statistics are calculated over the rainfall fields, interpolated into 0.775 × 0.775 km^2 reconstruction grid.

change in $\mathrm{NBias_t}$ due to missed low rain rate parts of the real rainfall field ($\mathrm{NBias_t}$ lowers from -0.05 to -0.08 over the whole coastal plain and from 0.06 to 0.00 in Tel-Aviv area, relatively to the 0.1 dB quantization simulation). Another counter-intuitive result is the decrease in $\mathrm{NRMSE_t}$ in Tel-Aviv area for 1 dB quantization simulation, relatively to 0.1 dB quantization simulation. It can be seen that the expression $r_t - r'_t$ in the numerator of Eq. (22) is equal to the expression for $\mathrm{Bias_s}(t)$ in Eq. (16). The reduction of positive $\mathrm{NBias_s}$ in Tel-Aviv area (see Table 3) due to missed weak rain rates in the case of 1 dB quantization simulation expresses in lower $\mathrm{NRMSE_t}$ in Table 4. In other words, the less biased reconstruction in terms of $\mathrm{NBias_s}$ leads to better areal averaged reconstruction in terms of $\mathrm{NRMSE_t}$ (and, of course, $\mathrm{NBias_t}$).

6. Summary and conclusions

We built a non-linear tomographic model over a variable density grid, aimed to overcome the challenges, imposed by adoption of a commercial microwave communication system and equipment for rainfall monitoring, and conducted a quantitative study of its performance by means of a simulation experiment using installation of a real microwave backhaul network and a SIRT-based tomographic inversion technique. We concentrated on three major issues, specific for typical commercial, rather than dedicated equipment: inhomogeneous distribution of frequencies among the links, density of the links that varies in space and quantization error. It was found that the major strength of our technique is its ability to provide accurate estimates (bias of less than 10%) of integrated amounts of near-the-ground rainfall over large territories (area of $3200\ \mathrm{km}^2$) and high spatial resolution rainfall measurement in an urban area (average correlation in space of up to 0.89 at a data-driven grid with average cell size of $5.7\ \mathrm{km}^2$). The weak sides of the technique are its limited accuracy due to low density of microwave links in sparse, rural regions and poor capability to measure weak rainfall rates (below $1\ \mathrm{mm\ h^{-1}}$) due to quantization errors of the standard commercial equipment. The future steps will be concentrated on (a) further development of the concept of the data-driven variable density grid and formulating objective criteria for the tree-growing procedure and stopping conditions and (b) a study towards a reconstruction technique, most suitable for the microwave rainfall tomography using commercial communication networks, since the bicubic interpolation of the results, obtained over the irregular grid is in fact an ad hoc post-processing procedure which is not necessarily optimal.

Acknowledgements

We deeply thank Y. Eisenberg, Y. Dagan, S. Mouallem and H. Pistiner (Cellcom), A. Shilva and E. Moshiev (Pelephone) for their cooperation and providing the microwave data, A. Arie (Meteo-Tech), A. Stupp (Tel-Aviv University) and H. Kutiel (Haifa University) for radar data. Special thanks to Oren Goldshtein for his useful comments. This research was funded in part by the Yeshaya Horowitz Association and the Porter School of Environmental Studies at Tel Aviv University. The authors are grateful to Hidde Leijnse and an anonymous reviewer for their comments and suggestions that helped us to improve an early version of the paper.

References

[1] Messer H, Zinevich A, Alpert P. Environmental monitoring by wireless communication networks. Science 2006;32:713.

[2] Leijnse H, Uijlenhoet R, Stricker J. Rainfall measurement using radio links from cellular communication networks. Water Resour Res 2007;43(3).

[3] Olsen R, Rogers D, Hodge D. The aR^b relation in the calculation of rain attenuation. IEEE Trans Antennas Propag 1978;26(2):318–29.

[4] Jameson A. A comparison of microwave techniques for measuring rainfall. J Appl Meteorol 1991;30(1):32–54.

[5] Atlas D, Ulbrich C. The physical basis for attenuation-rainfall relationships and the measurements of rainfall parameters by combined attenuation and radar methods. J Rech Atmos 1974;8:275–98.

[6] Atlas D, Ulbrich C. Path- and area-integrated rainfall measurement by microwave attenuation in the 1–3 cm band. J Appl Meteorol 1977;16(12):1322–31.

[7] Minda H, Nakamura K. High temporal resolution path-average rain gauge with 50-GHz band microwave. J Atmos Ocean Technol 2005;22(2):165–79.

[8] Holt A, Kuznetsov G, Rahimi A. Comparison of the use of dual-frequency and single-frequency attenuation for the measurement of path-averaged rainfall along a microwave link. IEE Proc Microwaves Antennas Propag 2003;150(5):315–20.

[9] Rahimi A, Holt A, Upton G, Cummings R. Use of dual-frequency microwave links for measuring path-averaged rainfall. J Geophys Res 2003;108:4467.

[10] Grum M, Kraemer S, Verworn H, Redder A. Combined use of point rain gauges, radar, microwave link and level measurements in urban hydrological modelling. Atmos Res 2005;77(1–4):313–21.

[11] Upton G, Holt A, Cummings R, Rahimi A, Goddard J. Microwave links: The future for urban rainfall measurement? Atmos Res 2005;77(1–4):300–12.

[12] Rahimi A, Holt A, Upton G, Krämer S, Redder A, Verworn H. Attenuation calibration of an X-band weather radar using a microwave Link. J Atmos Ocean Technol 2006;23(3):395–405.

[13] Krämer S, Verworn H, Redder A. Improvement of X-band radar rainfall estimates using a microwave link. Atmos Res 2005;77(1–4):278–99.

[14] Upton G, Cummings R, Holt A. Identification of melting snow using data from dual-frequency microwave links. IEE Proc Microwaves Antennas Propag 2007;1(2):282–8.

[15] Rincon R, Lang R. Microwave link dual-wavelength measurements of path-average attenuation for the estimation of drop size distributions and rainfall. IEEE Trans Geosci Remote Sens 2002;40(4):760–70.

[16] Giuli D, Toccafondi A, Biffi Gentili GA, Freni A. Tomographic reconstruction of rainfall fields through microwave attenuation measurements. J Appl Meteorol 1991;30(9):1323–40.

[17] Giuli D, Facheris L, Tanelli S. Microwave tomographic inversion technique based on stochastic approach for rainfall fields monitoring. IEEE Trans Geosci Remote Sens 1999;37(5):2536–55.

[18] Goldshtein O. Estimating space–time rainfall intensity using measurements from existing network of fixed terrestrial microwave links. Master's thesis, School of Electrical Engineering, Tel Aviv University; 2006.

[19] International Telecommunication Union Recommendation ITU-R P.838-2 Specific attenuation model for rain for use in prediction model; 2004.

[20] Berne A, Uijlenhoet R. Path-averaged rainfall estimation using microwave links: uncertainty due to spatial rainfall variability. Geophys Res Lett 2007;34(7):7403.

[21] Ciach G, Krajewski W. Analysis and modeling of spatial correlation structure in small-scale rainfall in Central Oklahoma. Adv Water Resour 2006;29(10):1450–63.

[22] Press W, Teukolsky S, Vetterling W, Flannery B. Numerical recipes in C: the art of scientific computing. Cambridge: Cambridge University Press; 1992.

[23] Kak A, Slaney M. Principles of computerized tomographic imaging. New York: IEEE Press; 1988.

[24] Ivansson S. Seismic borehole tomography – theory and computational methods. Proc IEEE 1986;74(2):328–38.

[25] Pinheiro P. Smoothness-constrained inversion for two-dimensional electrical resistance tomography. Measure Sci Technol 1997;8(3):293–302.

[26] Peña J, Lozano J, Larrañaga P. An empirical comparison of four initialization methods for the *K*-means algorithm. Pattern Recogn Lett 1999;20(10):1027–40.

[27] Amidror I. Scattered data interpolation methods for electronic imaging systems: a survey. J Electron Imag 2002;11(2):157–76.

[28] Nicholson SE, Some B, McCollum J, Nelkin E, Klotter D, Berte Y, et al. Validation of TRMM and other rainfall estimates with a high-density gauge dataset for West Africa. Part II. Validation of TRMM rainfall products. J Appl Meteorol 2003;42(10):1355–68.

[29] Xu B, Wikle C, Fox N. A kernel-based spatio-temporal dynamical model for nowcasting radar precipitation. J Am Stat Assoc 2005.